Chemical Engineering Journal 546 (2026) 180631

Contents lists available at ScienceDirect

Chemical Engineering Journal

journal homepage: www.elsevier.com/locate/cej

Phosphorization-pyrolysis engineered FeP@CNT heterostructures for efficient and durable direct seawater electrolysis☆

Samikannu Prabu [a,1], Giwon Lee [b,1], Mohan Reddy Pallavolu [c], Jinhan Cho [d], Yong Nam Ahn [a,*], Sungjun Park [e,f,**], Daegun Kim [a,*]

[a] School of Chemical, Biological and Battery Engineering, Gachon University, 13120, Seongnam, Republic of Korea
[b] Department of Chemical Engineering, Kwangwoon University, Seoul, 01897, Republic of Korea
[c] School of Chemical Engineering, Yeungnam University, Gyeongsan, 38541, Republic of Korea
[d] Department of Chemical and Biological Engineering, Korea University, Seoul, 02841, Republic of Korea
[e] Department of Electrical and Computer Engineering, Ajou University, Suwon, 16499, Republic of Korea
[f] Department of Intelligence Semiconductor Engineering, Ajou University, Suwon, 16499, Republic of Korea.

ARTICLE INFO

Keywords:
Metal-organic frameworks
FeP@CNT
Seawater electrolysis
Hydrogen evolution
Bifunctional electrocatalyst

ABSTRACT

Direct seawater electrolysis offers a sustainable pathway for hydrogen (H_2) production but is hindered by sluggish kinetics and severe chloride-induced corrosion. Here, we report a Phosphorization-Pyrolysis (PhosPy) strategy to construct a CNT-confined FeP heterostructure derived from a ZnFe metal-organic framework (MOF). During the PhosPy transformation, MOF-derived Fe species catalyze in situ CNT growth while simultaneously forming FeP, creating a strongly coupled FeP@CNT architecture with enhanced conductivity and structural stability. As a result, FeP@CNT-900 exhibits excellent bifunctional electrocatalytic activity in natural seawater, requiring only 74 mV for HER and 184 mV for OER to reach 10 mA cm^{-2}. A symmetric electrolyzer delivers 100 mA cm^{-2} at 1.49 V, outperforming the benchmark Pt/C||RuO_2 system, and maintains stable operation for over 1000 h at 500 mA cm^{-2} under practical conditions. Mechanistic analysis reveals a synergistic chloride-tolerant interface, where FeP preferentially adsorbs OH^- while the CNT scaffold restricts Cl^- diffusion. These findings establish a new catalyst design template integrating MOF-derived phosphide engineering, self-catalyzed CNT confinement, and interfacial ion regulation for efficient and durable H_2 production directly from seawater.

1. Introduction

The crucial need for sustainable and carbon-free energy sources has positioned hydrogen (H_2) as a leading candidate in the global energy transition. As a clean, high-energy-density fuel, H_2 can be produced via water electrolysis using renewable energy, thereby reducing fossil fuel dependence [1–3]. Although the thermodynamic potential for water splitting is 1.23 V, significant overpotentials are required due to sluggish kinetics of the HER and OER [4,5]. To overcome this, the development of robust metal-oxide-based electrocatalysts is crucial [6]. While noble metals such as Pt, Ru, and Ir-based oxides exhibit excellent catalytic activity, their high cost and scarcity limit their extensive deployment [7–9]. This has led to growing interest in transition metal-based compounds, especially phosphides, sulfides, oxides, and carbides, which offer cost-effective and scalable alternatives [10,11]. Iron phosphides, in particular, have shown promise due to their earth abundance, stability, and intrinsic bifunctionality for both HER and OER [12].

Alkaline seawater electrolysis is an emerging strategy that leverages seawater's natural alkalinity and abundance as an alternative electrolyte [11,13]. However, several challenges must be addressed, including chloride-induced corrosion, competitive side reactions (e.g., hypochlorite formation), and electrode degradation [14–16]. These challenges require electrocatalysts with high corrosion resistance, stable active sites, and efficient charge transport in saline environments. In this context, metal-organic frameworks (MOFs) have emerged as a highly tunable class of materials for electrocatalyst design, compared with

☆ This article is part of a Special issue entitled: 'Emerging Functional Materials' published in Chemical Engineering Journal.

* Corresponding authors.
** Correspondence to: S. Park, Department of Electrical and Computer Engineering, Ajou University, Suwon, 16499, Republic of Korea.
E-mail addresses: yahn@gachon.ac.kr (Y.N. Ahn), sj0223park@ajou.ac.kr (S. Park), daegunkim@gachon.ac.kr (D. Kim).

[1] The authors contributed equally to this work.

https://doi.org/10.1016/j.cej.2026.180631
Received 22 May 2026; Received in revised form 22 July 2026; Accepted 11 August 2026
Available online 11 August 2026

conventional catalyst synthesis strategies [17,18]. Their porous structure, large surface area, and compositional flexibility make them ideal precursors for functional materials [19]. Upon thermal transformation, MOFs can yield metal phosphides embedded in conductive carbon networks. For example, previous studies have reported Fe-MOF-derived RuCoP@CN and FeP@NPC electrocatalysts with enhanced HER/OER activity in alkaline media [20]. Similarly, the MOF-derived Fe_2P/Co_2P and CoP_3 nanosheets show bifunctional performance and chemical stability in simulated seawater [21].

A promising development is the construction of dual-phase iron phosphide-CNTs, where Fe_3P/Fe_2P and Ni_2P/Fe_2P phases are integrated with CNTs. This architecture combines the complementary catalytic properties of both phosphide phases with the exceptional conductivity and mechanical integrity of CNTs [22,23]. The resulting structure features a high density of exposed active sites, rapid electron transport pathways, and enhanced resistance to chloride-induced degradation. Recent work by Wang et al. demonstrated that FeP/CoP/NiP hybrid catalysts supported on CNTs delivered low overpotentials and stable bifunctional activity for overall water splitting in alkaline seawater [24–26]. The enhanced performance was attributed to the synergy between the dual-phase phosphides, the MOF-derived porous carbon matrix, and the CNT framework. Similarly, Li et al. developed a Fe-based phosphide-carbon hybrid catalyst exhibiting durable performance and high current densities under real seawater electrolysis conditions [27,28].

Seawater electrolysis under alkaline conditions (NaOH + NaCl) has demonstrated Faradaic efficiencies exceeding 99% using catalysts such as NiFe-LDH [29], NiFe/NiS [30], and NiMoN [31]. However, chloride-induced anode corrosion remains a major challenge for long-term operation. Cl^- ions strongly adsorb on polarized metal surfaces and form transient chlorine salts that subsequently convert to hydroxide precipitates, leading to irreversible dissolution of the active layer [32]. Although protective anions generated during catalyst oxidation or electrolyte design can temporarily slow Cl^- attack, their effectiveness is insufficient to ensure the long-term stability required for practical applications [33]. Moreover, most studies focus primarily on anodic degradation, often overlooking the coupled effects of anodic OER and cathodic HER under realistic seawater conditions [34]. Recently, metal phosphide-carbon hybrid catalysts have attracted increasing attention for seawater electrolysis due to their high intrinsic activity and corrosion resistance. Integrating multiphase phosphides within conductive carbon frameworks can provide abundant active sites, facilitate charge transport, and improve stability in chloride-rich environments. For instance, phosphide-carbon electrocatalysts such as NiFe-P@NC [35], C@CoP-FeP heterostructures [36], $NiCoFeMnCu)_2P/C$ [37], and mixed Ni_2P-Fe_2P [38], highlight the advantages of multiphase phosphide architectures in harsh electrolytes. Nevertheless, achieving simultaneous chloride resistance, rapid interfacial kinetics, and long-term stability at high current densities remains a significant challenge. Consequently, the rational design of CNT-confined phosphide heterostructures with intrinsic chloride tolerance is highly desirable.

Herein, we report a MOF-derived FeP NPs catalyst confined within an in situ grown conductive CNT scaffold, synthesized through a phosphorization-pyrolysis (PhosPy) transformation strategy, as a promising platform for chloride-resistant seawater electrocatalysis. During the PhosPy process, MOF-derived Fe species simultaneously catalyze CNT growth while forming FeP NPs, generating a strongly coupled FeP@CNT heterostructure. This integrated architecture enhances electronic conductivity, stabilizes FeP nanostructures, and promotes efficient charge transport across the FeP-CNT interface. In addition, phosphorus incorporation modulates the electronic structure, creating abundant catalytic sites and inducing charge redistribution. The formation of Lewis-acidic P-OH species further establishes a protective interfacial layer that suppresses chloride penetration and mitigates Cl^--induced corrosion. As a result, the FeP@CNT-900 heterostructure delivers excellent bifunctional catalytic activity for HER and OER in alkaline seawater while maintaining long-term operational stability.

2. Experimental section

2.1. Synthesis of ZnFe-MOF

In this synthesis, 0.249 g of zinc nitrate hexahydrate was dissolved in 25 mL of methanol. Separately, 0.328 g of 2-methylimidazole was dissolved in 25 mL of methanol. The 2-methylimidazole solution was then rapidly added to the zinc nitrate solution under vigorous stirring. The combined mixture was stirred continuously at room temperature (25 °C) for 30 min to ensure complete mixing. Subsequently, iron nitrate hexahydrate was introduced to the reaction mixture, which was then left undisturbed at room temperature for 5 h to allow for MOF formation. The resulting ZnFe-MOF precipitate was collected by centrifugation at 6000 rpm for 5 min, washed three times with methanol to remove impurities, and finally dried overnight in a vacuum oven at 60 °C to yield the final product.

2.2. Fabrication of FeP@CNT

The FeP@CNT catalyst was prepared using a combined phosphorization-pyrolysis method, referred to as the “PhosPy” process. The previously synthesized ZnFe-MOF was mixed with sodium dihydrogen phosphate (NaH_2PO_4) at various loadings (1, 2, 3, and 4 wt%). This mixture was then subjected to heat treatment under a nitrogen atmosphere at 900 °C for 2 h to obtain FeP@CNT-900-2. The resulting products were washed three times with 1 M HCl to remove residual metal species and other impurities. For comparison, additional samples were prepared at 800 °C, 850 °C, and 950 °C using the same procedure to assess the influence of temperature on catalyst properties.

For comparison, control samples were prepared without NaH_2PO_4 under the same pyrolysis conditions at 800, 850, and 950 °C, yielding non-phosphorized CNT-based products.

3. Results and discussion

3.1. Structure and morphology characterizations

The Dual-Phase FeP@CNT heterostructure was synthesized using a ZnFe-MOF as a sacrificial template to produce a porous structure (Scheme 1). The precursor underwent a single-step treatment involving simultaneous pyrolysis and phosphorization with NaH_2PO_4 under an inert atmosphere at elevated temperatures. This process resulted in the formation of FeP nanoparticles (NPs) embedded within a conductive carbon matrix. The pristine ZnFe-MOF precursor (Fig. S1) exhibits well-defined polyhedral microcrystals with smooth facets, indicative of high crystallinity and structural order. Following PhosPy treatment with 2 wt % NaH_2PO_4 at 800 °C (Figs. S2a,b), the framework collapses into densely packed NPs, with high-magnification imaging revealing residual MOF facets interspersed with newly formed FeP nanograins, suggesting incomplete transformation and limited CNT growth. At 850 °C (Figs. S2c,d), the morphology becomes more uniform, with smooth-surfaced particles and minimal polyhedral remnants, reflecting near-complete conversion to FeP NPs embedded in an amorphous carbon matrix. A distinct morphological transition occurs at 900 °C (Figs. S3a and b), where uniformly dispersed FeP NPs are anchored within a highly entangled CNT network, resulting in a porous and conductive three-dimensional architecture. This temperature optimally promotes CNT growth, maximizing active site exposure. At 950 °C (Fig. S3c,d), pronounced grain coarsening and the development of thick-walled CNTs are observed, indicating that excessive thermal energy facilitates particle aggregation, albeit with retention of the CNT framework. In contrast, 900 °C represents the optimal PhosPy temperature, achieving a balanced integration of NPs dispersion, CNT growth, and structural stability.

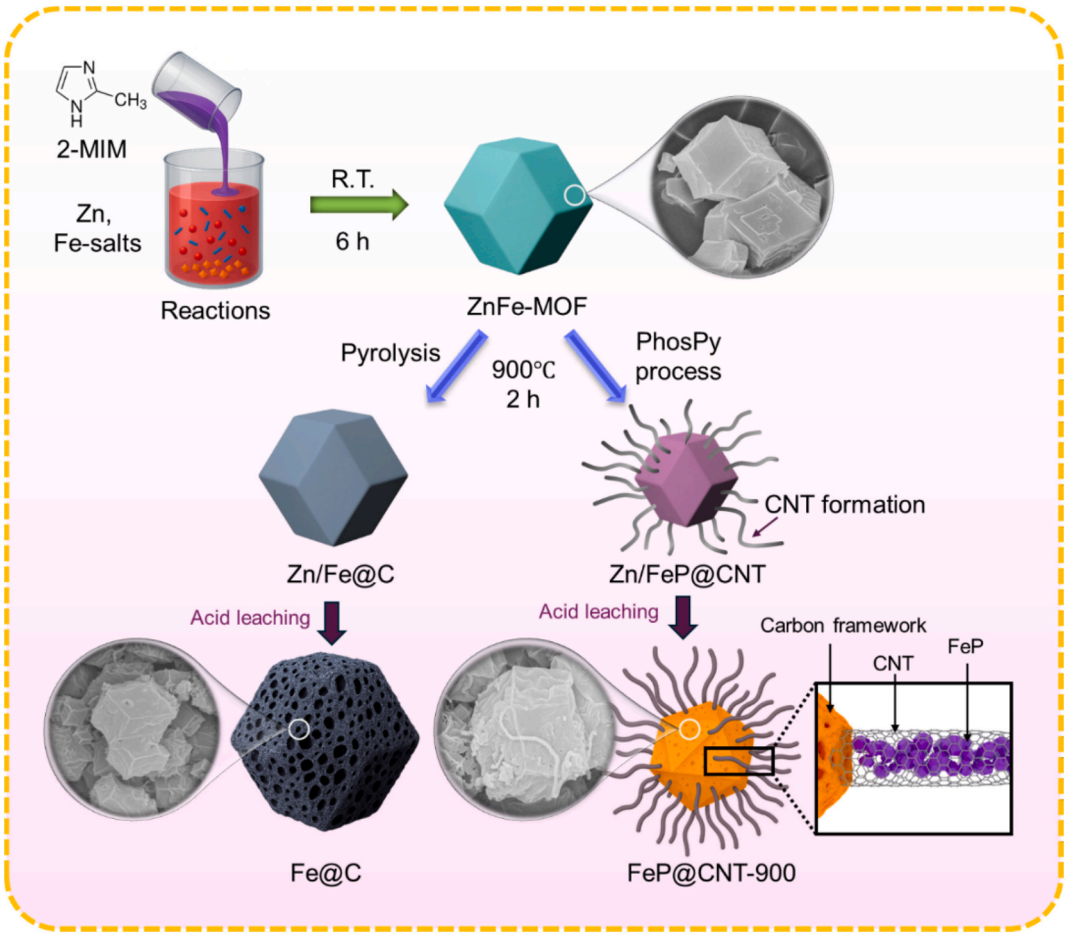

Scheme 1. Schematic illustration of the PhosPy synthesis of FeP@CNT derived from ZnFe-MOF.

In addition, the FE-SEM images clearly show the morphological evolution of ZnFe-MOF into FeP@CNT heterostructure through the PhosPy process at 900 °C with different NaH_2PO_4 loadings. As 1 wt% NaH_2PO_4 is introduced (Figs. S4a,b), the smooth polyhedral surfaces of the MOF become rough, and early-stage nanotube-like filaments start to appear, indicating the onset of catalytic carbon graphitization during phosphorization. At the optimal loading of 2 wt% NaH_2PO_4 (Figs. S4c, d), a dense CNT network forms, uniformly distributed and firmly anchored to the FeP NPs through in situ catalytic growth driven by MOF-derived carbon species. However, further increasing the NaH_2PO_4 content to 3–4 wt% (Figs. S5a-d) results in an overly dense CNT network accompanied by partial collapse of the original framework, caused by excessive phosphorization and sintering. This progression highlights the critical influence of NaH_2PO_4 content on dominating both CNT formation and structural preservation. The FE-SEM microstructures show the structural evolution of ZnFe-MOF into Fe@C-900 heterostructure via the pyrolysis process at different temperatures. In pristine ZnFe-MOF heat treatment (Figs. S6a-d), the particles largely retain their shape but develop rougher, more textured surfaces, indicating partial framework decomposition and carbonization.

The morphology and structure of the FeP@CNT hybrid were investigated by TEM, as shown in Fig. 1. TEM images (Fig. 1a,b) clearly reveal that FeP NPs are uniformly anchored onto the CNT framework without significant aggregation, while the CNTs retain their tubular structure, providing a conductive backbone. The HR-TEM image (Fig. 1c) displays distinct lattice fringes with interplanar spacings of 0.18 nm (Fig. 1c^1) and 0.34 nm (Fig. 1c^2), corresponding to the (200) plane of orthorhombic FeP NPs and the (002) plane of graphitic carbon, respectively, confirming the successful integration of crystalline FeP with CNTs. Fig. 1c1 and c2 show the HRTEM image and the corresponding line-intensity profile, revealing lattice spacings of ~0.18 nm, which can be attributed to the crystalline planes of FeP NPs. The CNT framework typically exhibits a graphitic (002) lattice spacing of ~0.34 nm, confirming the coexistence of FeP and CNT in the heterostructure. The intimate interface between FeP and CNTs is expected to facilitate rapid electron transfer during electrochemical reactions. The SAED pattern (Fig. 1d) further supports the polycrystalline nature of FeP NPs, as evidenced by the well-defined diffraction rings. Elemental mapping (Fig. 1e) demonstrates the uniform distribution of Fe, P, C, and N throughout the heterostructure, verifying the formation of FeP and its strong coupling with the CNT matrix.

The XRD pattern of the synthesized ZnFe-MOF (red curve) aligns well with the standard ZIF-8 pattern (black curve), confirming the successful formation of a ZIF-8-type crystalline structure (Fig. S7). Sharp peaks at characteristic 2θ positions such as 7.4°, 10.4°, 12.8°, 14.7°, 16.4°, and 18.0° indicate high crystallinity and long-range order. The absence of extra peaks from Fe-based oxides or other phases shows that Fe ions are successfully incorporated into the ZIF-8 lattice without altering its topology, preserving the sodalite framework.

The XRD pattern confirms the formation of mixed iron phosphide phases (Fe_2P/Fe_3P@CNT) embedded within the CNT matrix. Among them, sharp and intense diffraction peaks corresponding to Fe_3P dominate, suggesting it is the primary crystalline phase [39], which crystallizes in a tetragonal system (space group I-4, No. 82). The main reflections at $2\theta \approx 40.8°$, 44.2°, and 47.2° are indexed to the (112), (211), and (301) planes of Fe_3P, confirming it as the dominant phase. The narrow full-width at half-maximum (FWHM) of these peaks indicates high crystallinity and a well-defined lattice structure. In

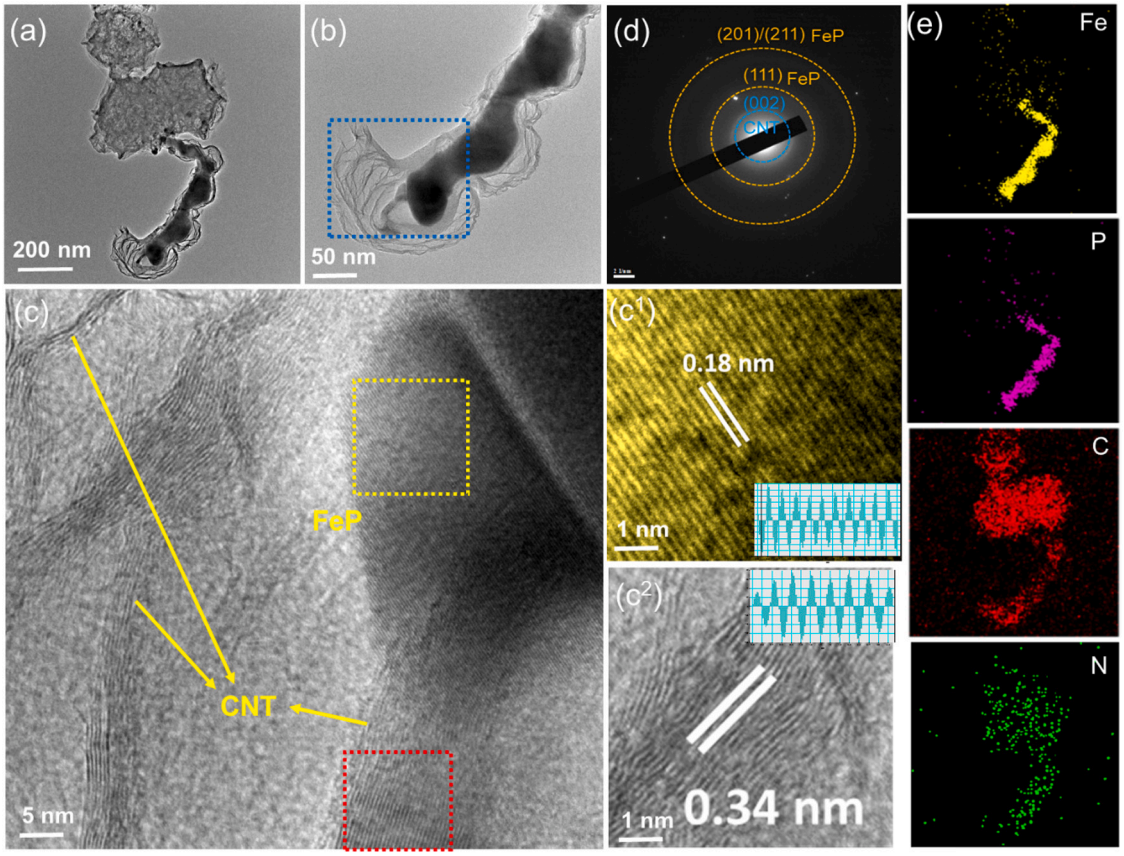

Fig. 1. TEM images of FeP@CNT-900-2; (a,b) TEM images, (c) HRTEM image with corresponding line-intensity profiles (c^1, c^2), (d) SAED pattern, and (e) TEM-EDS mapping.

addition, minor peaks observed near 30.0°, 40.0°, and 54.5° correspond to Fe_2P (hexagonal structure, space group P-62 m, No. 189), indexed to the (110), (211), and (300) planes, respectively (Fig. 2a). Their presence signifies Fe_2P as a secondary phase, reflecting partial or incomplete phosphidation during synthesis, which may affect the material's electrochemical and catalytic properties. Additionally, a broad, weak peak centered at 26.3° corresponds to the (002) plane of graphitic carbon. The broadness suggests a disordered or amorphous carbon phase derived from residual or introduced carbonaceous material.

The surface composition of FeP@CNT-900-2 was examined in detail using X-ray photoelectron spectroscopy (XPS) (Fig. S8). The Fe 2p XPS spectrum of FeP@CNT-900-2 exhibits a characteristic spin-orbit doublet corresponding to Fe $2p_{3/2}$ and Fe $2p_{1/2}$ located at approximately 711.0 eV and 724.5 eV, respectively (Fig. 2b) [40]. These peaks mainly arise from Fe—P bonding in the FeP lattice, where Fe exists in a slightly positive electronic state ($Fe^{\delta+}$) due to charge transfer with phosphorus. Minor components at slightly higher binding energies can be attributed to surface Fe^{2+}/Fe^{3+} species, likely formed by slight oxidation upon air exposure. The weak satellite peaks at ~719.0 eV and ~ 732.5 eV further indicate a small fraction of oxidized Fe species. The P 2p spectrum exhibits a primary doublet composed of P $2p_{3/2}$ and P $2p_{1/2}$ located near 129.5 eV and 130.3 eV, respectively [41], corresponding to phosphorus bonded to metal (Fe—P), a hallmark of transition metal phosphides (Fig. 2c). A broader peak around 133.5 eV is attributed to oxidized phosphorus species, such as P—O or phosphate groups, which may form on the surface due to air exposure. This surface oxidation is common in phosphide systems and may create a beneficial core-shell structure, where the inner Fe—P core remains active, and the outer oxide layer facilitates proton transport. A main peak at approximately 284.8 eV, attributed to graphitic sp^2-hybridized carbon from the CNT backbone (Fig. 2d), dominates the C 1 s spectrum. Additional peaks at around 285.6 eV and 288.5 eV are assigned to C—O and O-C=O functional groups, respectively, suggesting partial surface oxidation or functionalization of the CNTs. The oxygen-containing groups can improve hydrophilicity and enhance the dispersion of active dual-phase FeP NPs. The O 1 s spectrum (Fig. 2e) displays a broad envelope that can be deconvoluted into at least three components. The main peak at 530.1 eV corresponds to lattice oxygen, possibly from iron oxides or surface phosphates. A second peak at 531.5 eV is related to oxygen in hydroxyl or adsorbed water species, while the third peak around 533.2 eV may stem from carbon-oxygen species (C-O-C or COOH), which aligns with the C 1 s results. The high-resolution N 1 s XPS spectrum displays multiple deconvoluted peaks, indicating various nitrogen bonding environments. The peak at ~398.3 eV corresponds to pyridinic-N, which enhances catalytic activity by donating lone-pair electrons to metal centers. The ~399.6 eV peak is assigned to pyrrolic-N, contributing to conductivity and active site exposure (Fig. 2f). The ~400.8 eV peak indicates graphitic-N, integrated into the carbon lattice to boost electron mobility. A weaker peak near ~402.4 eV represents oxidized nitrogen species (N—O), likely formed during air exposure after synthesis.

Fig. S9 presents the FTIR spectra of Zn-MOF, ZnFe-MOF, and FeP@CNT-900-2. The pristine Zn-MOF and ZnFe-MOF show a set of well-defined vibrational bands that are characteristic of synchronized organic linkers and metal-oxygen natures. The many absorption descriptions between ~1600 and 1000 cm^{-1} correspond to the C=O, C=C, and C—O stretching modes characteristically related to the imidazole-based MOF backbone. The introduction of Fe into Zn-MOF produces obvious changes in the intensity and relative positions of these peaks, indicating alteration of the coordination environment and partial modification of the metal nodes. In contrast, FeP@CNT-900 shows a broad and feature-poor spectrum, dominated by an almost monotonic trend without the distinct ligand-related signals seen in the

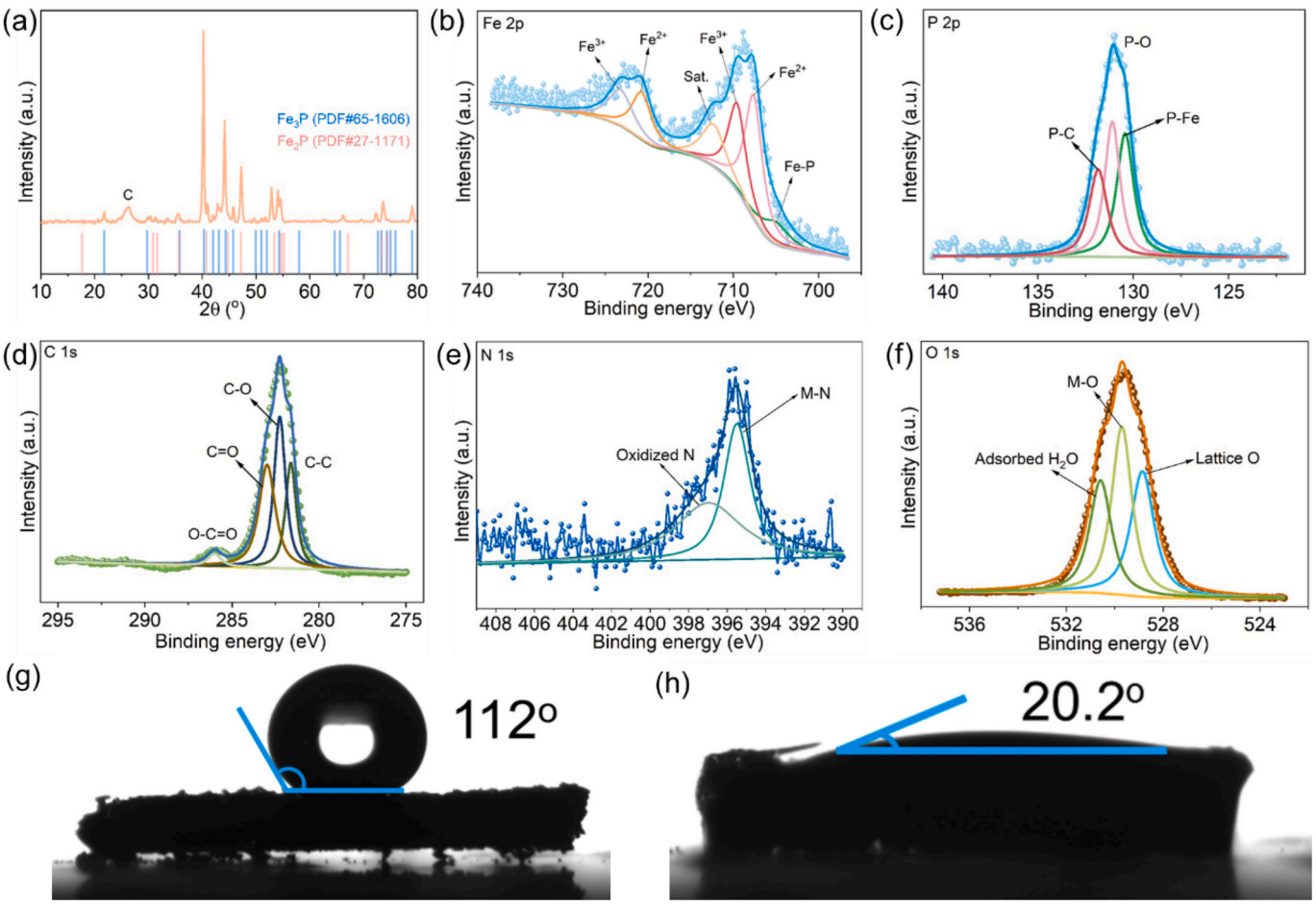

Fig. 2. (a) XRD pattern, high-resolution XPS of (b) Fe 2p, (c) P 2p, (d) C 1 s, (e) O 1 s, and (f) N 1 s of the FeP@CNT-900-2 and water contact angle of (g) ZnFe-MOF and (h) FeP@CNT-900-2.

MOFs. This displays the complete decomposition of the organic framework during pyrolysis and the formation of a CNT-rich structural design. The absence of specific MOF peaks, combined with the efficient spectral profile, is stable with graphitized carbon domains embedding FeP NPs.

Fig. S10 exhibits the Raman spectra of the FeP@CNT-900-2 sample, in which the characteristic D (1353 cm^{-1}) and G (1605 cm^{-1}) bands are observed. The D band originates from defect-related vibrational modes and structural irregularities inside the carbon framework, whereas the G band corresponds to the ordered sp^2 domains of graphitic carbon. The measured I_D/I_G ratio of 0.84 specifies a balanced combination of graphitization and defect density. This level of arranging is required for carbon materials exposed to high-temperature treatment, while the remaining disorder reflects the influence of Fe—P species and heteroatom incorporation during the pyrolysis process. Such a mixed structural nature, graphitic zones linked with defect-rich sites, promotes efficient electron transport along the CNT network and simultaneously offers abundant anchoring points for nanoscale FeP NPs.

Based on the XPS discussion, there is strong electronic interaction between FeP NPs and the surrounding CNT network. Their profound interaction drives interfacial charge redistribution, producing electron-rich Fe sites and electron-deficient P sites, consistent with the shifts examined in the Fe 2p and P 2p XPS spectra. This polarization effectively tunes the surface electronic structure of FeP, making its active sites more responsive during catalysis. P—C coordination at the interface further stabilizes the FeP phase and initiates a highly efficient electronic link to the CNT framework. This connection enables rapid electron transfer through the CNT backbone, ensuring that electrons reach the FeP surface with minimal loss and supporting faster catalytic turnover. It highlights the complementary roles of each component: CNTs act as a fast electron-transport scaffold, while FeP provides the catalytically active centers. The wettability of the catalysts strongly influences their seawater splitting performance. ZnFe-MOF shows a contact angle of 112°, suggesting poor electrolyte penetration and sluggish bubble release, which limit active site utilization. In contrast, FeP@CNT-900-2 exhibits a much lower angle of 20.2°, indicating excellent hydrophilicity that promotes fast ion diffusion, charge transfer, and gas desorption (Fig. 2g,h).

The nitrogen adsorption-desorption isotherms and corresponding pore-size distributions provide insight into the structural evolution during the MOF-to-phosphide conversion (Fig. S11). Both Zn-MOF and ZnFe-MOF exhibit typical type-IV isotherms, confirming mesoporous structures. Zn-MOF shows a high BET surface area of 1864.99 $m^2\ g^{-1}$ with a pore volume of 0.695 $cm^3\ g^{-1}$, while ZnFe-MOF retains substantial porosity (1608.21 $m^2\ g^{-1}$, 0.641 $cm^3\ g^{-1}$), providing a porous template for subsequent phosphide formation. After phosphorization, FeP@CNT-900-2 displays a reduced surface area (345.63 $m^2\ g^{-1}$) and pore volume (0.345 $cm^3\ g^{-1}$), reflecting structural densification caused by FeP crystallization and CNT integration. Despite the decrease in surface area, FeP@CNT-900-2 maintains hierarchical micro-mesoporous structures, with micropores derived from the MOF framework and interconnected mesopores centered at 12–18 nm, which facilitate electrolyte diffusion and ion transport. The CNT-confined architecture stabilizes FeP nanoparticles and maintains open pathways for electrolyte diffusion. The hierarchical porosity and conductive network promote efficient charge transfer and mass transport, enhancing electrocatalytic performance [42,43].

3.2. Electrocatalytic alkaline seawater splitting

The OER performance of the catalysts was initially evaluated in an O_2-saturated 1 M alkaline seawater (ASW) electrolyte using a standard three-electrode configuration. As shown in Fig. 3a, the linear sweep voltammetry (LSV) curves reveal that FeP@CNT-900-2 exhibits the lowest onset potential and delivers the highest current density across the entire potential range, outperforming both ZnFe-MOF and Fe@C-900. This enhanced activity is attributed to the formation of catalytically active FeP species, as well as the development of a conductive CNT network during the high-temperature treatment.

Among the synthesized catalysts, FeP@CNT-900-2 shows outstanding OER activity, requiring only 184 mV of overpotential to reach a current density of 10 mA cm^{-2} (Fig. 3b). This value is much lower than Fe@C-900 (233 mV) and ZnFe-MOF (278 mV), highlighting its superior electrocatalytic performance (Table S2). The significantly reduced overpotential indicates more efficient charge transfer and lower energy barriers for driving the OER. CV analysis (Fig. S12) further confirms this improvement, with FeP@CNT-900-2 showing distinct FeP oxidation peaks, which suggest easy access of electrolyte species to the FeP active sites through the nanochannels created by the porous, defective carbon shell [35]. Moreover, the catalytic activity of FeP@CNT-900-2 was optimized by systematically varying phosphorus content, reaction temperatures in the PhosPy process (Fig. S13), and NaH_2PO_4 loading ratios (Fig. S14). These optimization steps helped achieve an ideal microstructure and surface composition, further boosting the material's OER kinetics. The Tafel plots derived from the LSV curves display that FeP@CNT-900-2 possesses the smallest Tafel slope of 41.2 mV dec^{-1}, indicating its fast reaction kinetics compared to Fe@C-900 and ZnFe-MOF (Fig. 3c). This shows a faster rate-determining step during OER, likely due to the synergistic effect between the FeP NPs and the CNT matrix. The improved electron transport and reduced kinetic barriers at the electrode-electrolyte interface are critical for achieving efficient water oxidation. EIS measurements were conducted to probe the interfacial charge transfer characteristics of the catalysts during the OER in ASW. The Nyquist plots were fitted using a simplified Randles circuit model to extract the solution resistance (R_s) and charge transfer resistance (R_{ct}). Among the samples, FeP@CNT-900-2 exhibited the lowest R_{ct} value (≈ 12.8 Ω), significantly lower than Fe@C-900 (≈ 24.3 Ω) and ZnFe-MOF (≈ 38.5 Ω), indicating more efficient interfacial electron transfer during the OER process (Fig. S15). The reduced R_{ct} for FeP@CNT-900-2 can be attributed to the enhanced electrical conductivity provided by the interconnected CNT framework and the highly dispersed Fe—P active sites. The solution resistance (R_s) remained

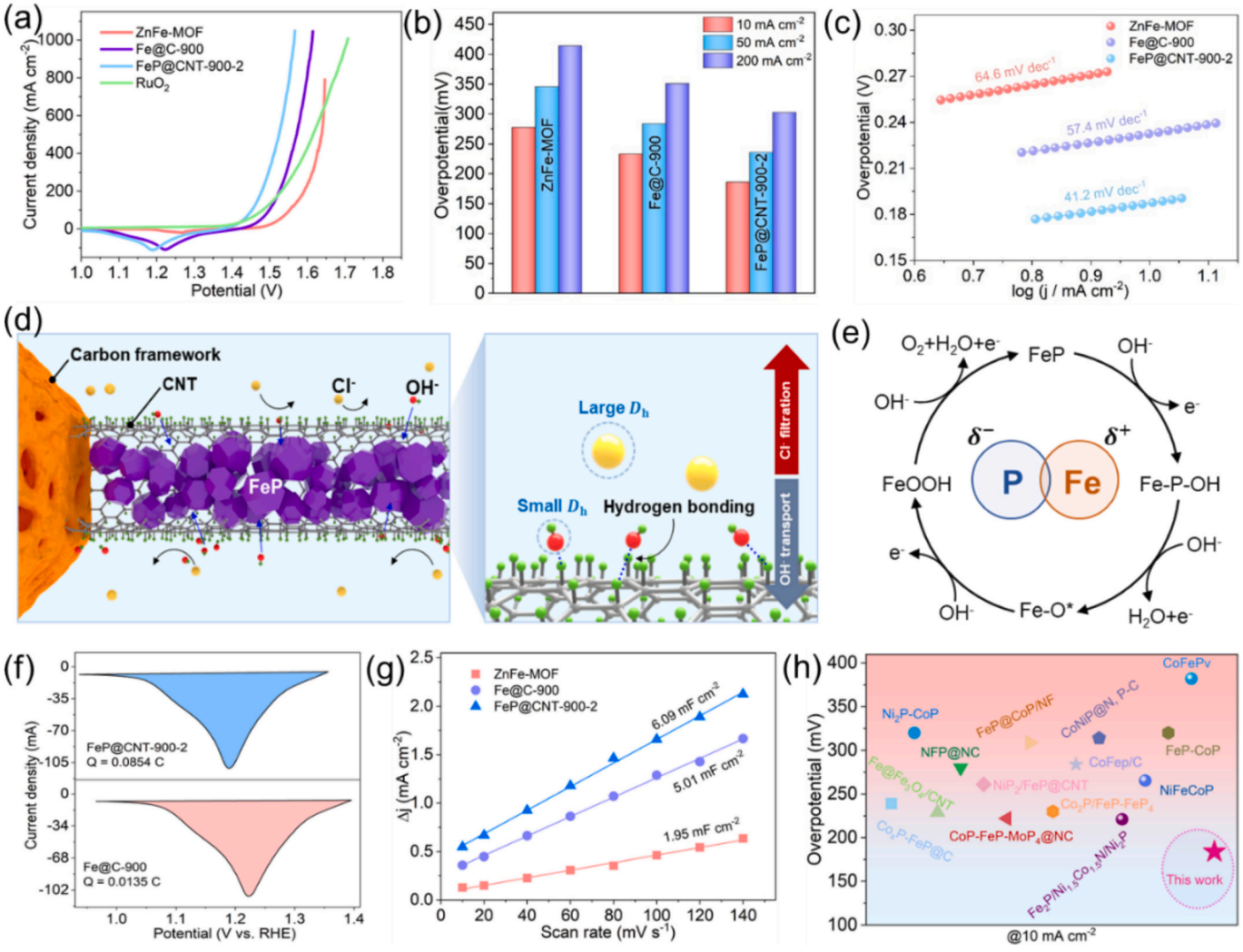

Fig. 3. Electrocatalytic OER performance in alkaline seawater. (a) LSV curves (90% iR correction) of FeP@CNT-900-2, Fe@C-900, and ZnFe-MOF, (b) overpotential, and (c) Tafel plot derived from the LSV curves in (a). (d) Possible reaction and properties between OH^- diffusion and Cl^- suppressed, (e) OER multiple-step mechanism on FeP@CNT-900-2. (f) Reductive current obtained from the CV curves recorded at a scan rate of 5 mV s^{-1} within the potential range of 0.85–1.4 V vs RHE, (g) C_{dl} curves, and (h) Comparison of the overpotentials required to achieve current densities of 10 mA cm^{-2} in 1 M KOH + seawater for FeP@CNT-900-2, alongside those of recently reported catalysts.

similar for all samples, ranging from 1.9 to 2.2 Ω, confirming stable electrolyte conductivity and consistent electrode contact. The conclusions correlate well with the observed lower overpotentials and Tafel slopes for FeP@CNT-900-2, highlighting its superior OER catalytic performance.

The electrocatalytic OER performance of FeP@CNT-900-2 was evaluated in both 1.0 M KOH and 1.0 M alkaline seawater electrolytes. To avoid interference from the strong oxidation peaks of nickel foam, the LSV curves were recorded by scanning the potential negatively, preventing overlap between the nickel oxidation signals and the OER activity of the catalysts. As shown in Fig. S16, FeP@CNT-900-2 exhibits comparable OER activity in 1 M KOH + seawater and in 1 M KOH. The consistent catalytic performance through various electrolytes highlights the protective role of the CNT, which effectively safeguards the active FeP NPs sites against seawater. In addition, the EIS analysis, shown as Nyquist plots, compares the charge transfer behavior of FeP@CNT-900-2 electrodes in 1.0 M KOH and 1.0 M KOH with seawater (Fig. S17). Both EIS exhibit similar arc diameters in the high-frequency region, indicating R_{ct} values of about 11.2 Ω for KOH and 11.8 Ω for seawater. This small difference confirms that seawater ions do not notably hinder electron transfer during OER. In the low-frequency region, a linear Warburg element indicates efficient ion diffusion in both electrolytes. Equivalent circuit fitting shows comparable solution Rs values around 2.1 Ω (KOH) and 2.3 Ω (seawater).

The ion-selective activity of FeP@CNT-900-2 in alkaline seawater electrolysis is managed by a coupled hydration-adsorption-diffusion mechanism. Upon electrochemical activation, the phosphide surface recreates into a thin FeOOH/$FePO_x$ layer, featuring coordinatively unsaturated Fe sites and an oxygen-rich environment [44]. OH^-, possessing a reduced effective hydration radius and a flexible hydrogen-bond network, can readily undergo partial dehydration and chemisorb onto Fe regions via inner-sphere Fe-OH bonding [45]. This chemisorption enables rapid interfacial diffusion through continuous bond exchange during the OER process [46–48]. In contrast, Cl^- exhibits a larger and more rigid hydration shell and lower interfacial mobility, which requires a high dehydration barrier and restricts its interaction to weak outer-sphere physisorption [49]. As a result, Cl^- diffusion is limited to the outer electric double layer and does not penetrate or migrate along the reconstructed layer. The hierarchical porosity further facilitates OH^- transport while limiting chloride diffusion by shortening OH^- transport routes, though proposing no energetic advantage for hydrated chloride ions [50]. (Fig. 3d). Under anodic preference, the FeP surface transforms into an amorphous FeOOH layer enriched in Fe^{3+} sites [51,52], which provide balanced adsorption-desorption energies for oxygenated intermediates, thus assisting the four-electron OER pathway (Fig. 3e). Through this process, P atoms act as electronic mediators by coupling Fe redox centers with the CNT scaffold interactions. The defect-rich P sites at the FeP-CNT interface hybridize with the sp^2-carbon network, developing identified states that facilitate fast electron transfer to the current collector. Additionally, P incorporation modulates the Fe electronic configuration, lowering the activation barrier for redox cycling and enhancing water adsorption and intermediate stabilization. The OER pathway progresses via OH^- adsorption on Fe^{3+} to form *OH, deprotonation to *O, nucleophilic attack by OH^- to yield *OOH, and O—O bond formation followed by O_2 release (Fig. 3e) [53]. During operation, Fe_2P/Fe_3P rapidly reconstructs as OH^- attack forms Fe-P-OH species into FeOOH, while P oxidizes to surface P-O_x [54]. The oxidized P layer also controls chloride adsorption, yielding a stable and cooperative FeOOH/P-O_x interface that enhances activity and durability. The proposed OH^-/Cl^- selectivity and surface reconstruction mechanisms (Fig. 3d,e) are based on the interfacial electronic interaction between FeP and the conductive CNT framework. Previous studies have reported that metal phosphides undergo surface reconstruction under alkaline electrochemical conditions, forming catalytically active oxyhydroxide species that facilitate OH^- adsorption while suppressing competitive Cl^- adsorption [55]. In addition, the strong electronic coupling at heterogeneous interfaces can induce charge redistribution, thereby modulating adsorption energies of reaction intermediates and improving reaction selectivity [56].

The CV curves of FeP@CNT-900-2 and Fe@C-900 highlight the superior electrochemical properties of the CNT-supported catalyst. FeP@CNT-900-2 exhibits a much higher charge (Q = 0.0854C) compared to Fe@C-900 (Q = 0.0135C), indicating a larger electrochemically active surface area (Fig. 3f). The wider CV profile and higher current response confirm faster electron transfer and stronger redox activity. As shown in Fig. S18, the double-layer capacitance (C_{dl}) was determined to estimate the electrochemically active surface area (ECSA) of the catalysts. Among the tested samples, FeP@CNT-900-2 exhibited the highest C_{dl} value of 6.09 mF cm^{-2} (Fig. 3g), indicating a significantly larger electrochemically active region. In comparison, Fe@C-900 and ZnFe-MOF displayed lower C_{dl} values of 5.01 mF cm^{-2} and 1.95 mF cm^{-2}, respectively, reflecting a reduced number of available active sites. Based on the measured C_{dl} values (Fig. 3g), the corresponding ECSA values were calculated. FeP@CNT-900-2 achieved an ECSA of 152 cm^2, which is substantially higher than that of Fe@C-900 (126 cm^2) and ZnFe-MOF (49 cm^2), further confirming its superior exposure of active sites for catalysis (Fig. S19). FeP@CNT-900-2 exhibits outstanding OER durability, sustaining 500 mA cm^{-2} in alkaline seawater for 200 h with no measurable loss in activity (Fig. S20). LSV profiles recorded before and after stability testing show negligible deviation (Fig. S21), indicating that the catalyst's active sites, electronic pathways, and structural framework remain intact. Furthermore, FeP@CNT-900-2 outperforms other reported transition metal-based OER catalysts in terms of catalytic activity (Fig. 3h and Table S2). This robustness derives from the FeP-CNT heterointerface, which maintains conductivity and stabilizes the FeOOH surface during long-term operation.

The Tafel polarization curves (Fig. S22a) confirm that FeP@CNT-900-2 delivers the most favorable HER kinetics in alkaline seawater, showing the lowest overpotential, highest current density, and a more positive onset potential compared to ZnFe-MOF and Fe@C-900. Its steeper Tafel slope reflects faster charge transfer and reduced kinetic barriers. This superior activity stems from the synergistic CNT-FeP heterostructure, where the CNT framework facilitates rapid electron transport and an enlarged surface area, while the FeP shell forms an OH^--anchored phosphate-chloride exchange shield that simultaneously accelerates HER and suppresses corrosion. In addition, the heterostructure Fe_3P/Fe_2P@CNT catalyst provides an intrinsic self-protective mechanism that is highly advantageous for alkaline seawater splitting. When exposed to the alkaline electrolyte, the FeP domains undergo surface activation, releasing phosphate species (PO_4^{3-}) in situ (Fig. S22b). Phosphate species act as dynamic shields, creating a phosphate-chloride exchange interface. At the molecular level, the OH^- anions preferentially adsorb onto the FeP NPs surface, which promotes the generation of phosphate groups. The phosphate ions compete directly with aggressive chloride ions (Cl^-) from seawater. Because of their stronger adsorption and coordination with Fe centers, PO_4^{3-} ions effectively displace incoming Cl^- ions, thereby forming a robust ion-exchange shield that suppresses chloride penetration. This mechanism prevents structural degradation of the catalyst and mitigates pitting corrosion that normally occurs in chloride-rich environments. Additionally, the CNT backbone serves a dual function by forming a hydrophobic microenvironment that blocks Cl^- ingress while simultaneously providing a conductive network for efficient electron transport. The phosphate-based surface offers synergistic protection, presenting excellent chloride tolerance and long-term stability during seawater electrolysis.

3.2.1. *Electrocatalytic HER alkaline seawater splitting*

The electrochemical performance of the catalysts toward the HER in seawater was systematically evaluated. In the LSV polarization curves (Fig. 4a), FeP@CNT-900-2 exhibits a markedly lower overpotential compared to Pt/C, Fe@C-900, and the pristine ZnFe-MOF precursor,

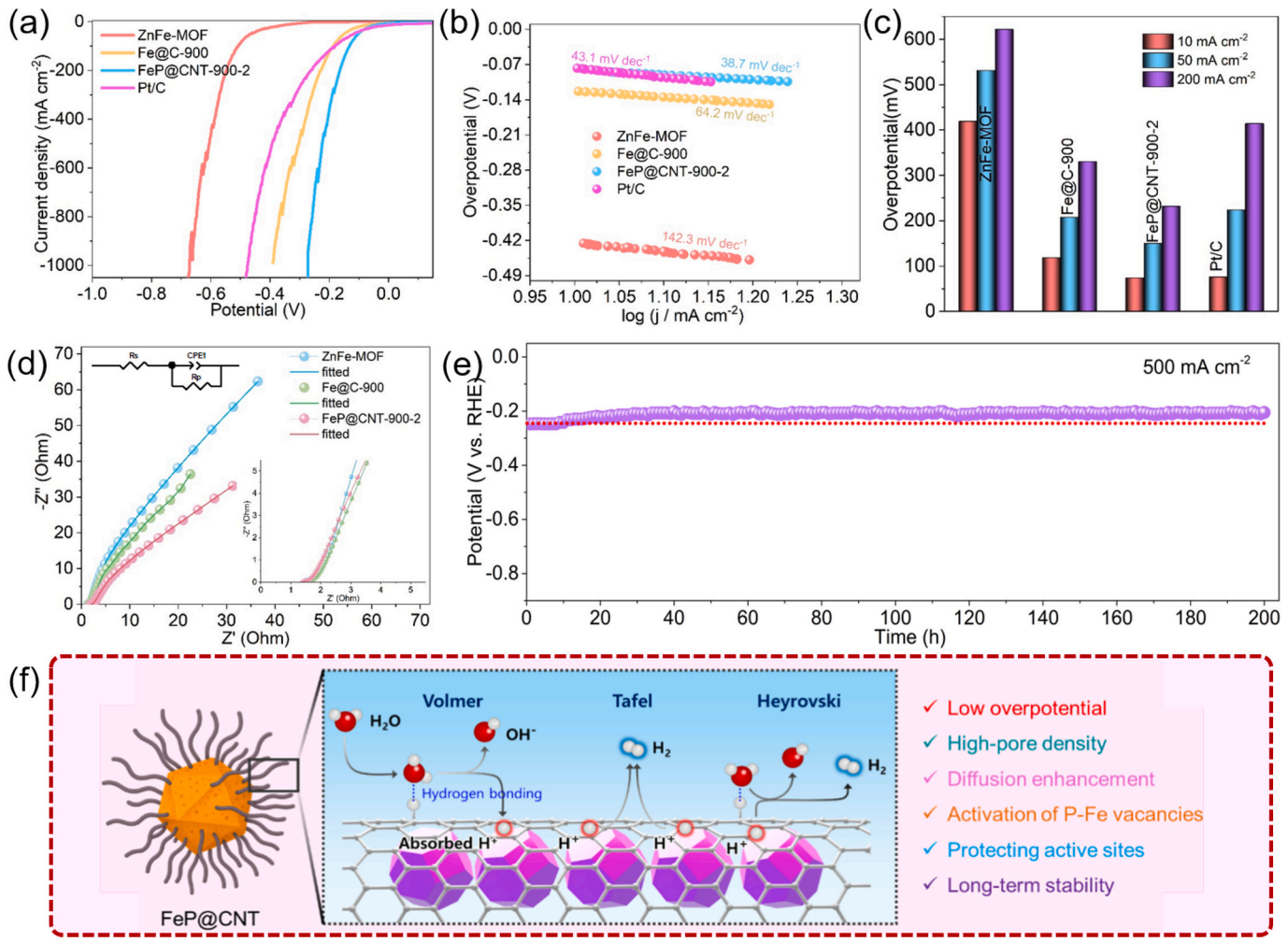

Fig. 4. HER electrochemical performance in direct alkaline seawater. (a) LSV curves (90% iR correction) of FeP@CNT-900-2, Fe@C-900, and ZnFe-MOF, (b) Tafel plot, (c) overpotentials, and (d) EIS spectra. (e) Durability test by chronoamperometry and (f) proposed HER reaction mechanism in direct alkaline seawater using FeP@CNT-900-2.

achieving the target current density at a substantially reduced voltage. This enhancement is ascribed to the synergistic coupling between the conductive CNT network and catalytically active FeP nanophases, which collectively promote rapid charge transfer and efficient proton reduction at the electrode-electrolyte interface. Varying the PhosPy temperature process (Fig. S23) and NaH_2PO_4 content confirmed that 900 °C with 2 wt % NaH_2PO_4 yielded the best activity (Fig. S24). The corresponding Tafel slopes (Fig. 4b) further confirm the superior kinetics of FeP@CNT-900-2, with a slope of 38.7 mV dec^{-1}, much lower than those of Pt/C (43.1 mV dec^{-1}), Fe@C-900 (64.2 mV dec^{-1}), and ZnFe-MOF (142.3 mV dec^{-1}). This indicates that FeP@CNT-900-2 undergoes the Volmer-Heyrovsky reaction mechanism, where the rate-determining step is the Heyrovsky step: the adsorbed hydrogen atom on the metal active site (M-H_{ads}) reacts with water and an electron to produce H_2, regenerate the metal site (M), and release hydroxide ions (OH^-).

Among synthesized catalysts, FeP@CNT-900-2 delivers the most outstanding HER performance, achieving a current density of 10 mA cm^{-2} at an overpotential of only 74 mV (Fig. 4c). This value is slightly lower than that of commercial Pt/C (76 mV) and substantially better than Fe@C-900 (119 mV) and ZnFe-MOF (419 mV). Such a remarkably low overpotential indicates superior intrinsic catalytic activity, rapid electron transfer, and minimal kinetic resistance, enabling highly efficient H_2 generation in alkaline seawater (Table S3). The charge transfer resistance (R_{ct}) of the catalysts was evaluated using the Nyquist plot (Fig. 4d). Among all the samples tested, FeP@CNT-900-2 exhibited the lowest R_{ct} value of 1.37 Ω, indicating superior electrical conductivity and faster charge transfer kinetics. In contrast, Fe@C-900 (1.89 Ω) and ZnFe-MOF (2.01 Ω) exhibited higher resistances, indicating slower electron transport in these materials. The significantly reduced R_{ct} for FeP@CNT-900-2 can be attributed to its well-integrated heterostructure, which enhances interfacial contact and facilitates efficient electron transfer. As shown in Fig. S25a-c, the double-layer capacitance (C_{dl}) was measured to estimate the electrochemically active surface area (ECSA). Among the catalysts tested, FeP@CNT-900-2 exhibited the highest C_{dl} value of 8.85 mF cm^{-2} (Fig. S25d), indicating a significantly larger electrochemically active region. In comparison, Fe@C-900 and ZnFe-MOF exhibited lower C_{dl} values of 4.47 mF cm^{-2} and 1.59 mF cm^{-2}, respectively, indicating fewer accessible catalytically active sites. The ECSA was calculated using the equation: C_{dl}/Cs, where Cs is the specific capacitance of a flat, smooth surface, typically taken as 0.040 mF cm^{-2} in 1 M KOH electrolyte. Based on this calculation, FeP@CNT-900-2 demonstrated the largest ECSA of 221 cm^2, significantly exceeding those of Fe@C-900 (112 cm^2) and ZnFe-MOF (40 cm^2), as depicted in Fig. S26. The superior ECSA of FeP@CNT-900-2 arises from its heterostructure design, which enhances the exposure of active sites.

The long-term electrochemical stability of the FeP@CNT-900-2 catalyst was assessed in alkaline seawater via chronopotentiometry. As shown in Fig. 4e, the catalyst sustained a stable current density of 500 mA cm^{-2} for an extended duration of 200 h, exhibiting negligible performance degradation (Table S3). Furthermore, the polarization curves

recorded after 200 h (Fig. S27) closely overlap with the initial curves, demonstrating minimal loss in catalytic activity. The results confirm the outstanding durability and operational stability of FeP@CNT-900-2 for the HER under harsh alkaline seawater. The catalytic process proceeds through three sequential stages. In the Volmer step, water molecules absorb onto FeP active sites embedded within the conductive CNT network. Electrons, efficiently transported through the CNT framework, reduce water to form surface-bound hydrogen species (M-H_{ads}) and release hydroxide ions (OH^-) into the electrolyte (Fig. 4f). In the surface diffusion step, the FeP-CNT interface facilitates hydrogen migration and coupling; the adsorbed hydrogen atoms migrate across the FeP surface and combine to form molecular H_2 before desorption. This step is promoted by the intimate FeP-CNT interface, which lowers the migration barrier and stabilizes hydrogen intermediates. The conductive CNT network facilitates efficient electron transfer, promoting the reaction kinetics. This mechanism is consistent with reported HER pathways for transition-metal phosphide catalysts [57]. Finally, in the Heyrovsky step, the remaining M-H_{ads} species react with water and an incoming electron, releasing additional H_2 and regenerating the active sites [58,59]. The synergistic integration of FeP and CNT ensures optimized hydrogen adsorption energy, rapid charge transfer, and sustained active site accessibility, resulting in superior catalytic activity and stability.

3.2.2. Overall seawater splitting

FeP@CNT-900-2 develops as an effective dual-functional electrocatalyst, delivering remarkable performance and durability for overall water splitting. Fig. 5a shows a symmetric two-electrode seawater electrolyzer, where FeP@CNT-900-2 is used as both the cathode (HER) and anode (OER). In this system, FeP NPs are uniformly anchored on CNTs, establishing a highly interconnected system that accelerates efficient electron transport while maintaining strong structural integrity. The polarization curves show that the FeP@CNT-900-2‖FeP@CNT-900-2 electrolysis achieves a current density of 100 mA cm^{-2} at a remarkably low cell voltage of 1.49 V, significantly outperforming the benchmark Pt/C‖RuO_2 system (1.68 V) (Fig. 5b). This significantly lower operating voltage highlights the superior catalytic activity of the FeP@CNT-900-2. The sharp rise in current density at low voltages further points to highly favorable HER kinetics, which can be attributed to the minimal energy barrier associated with the Volmer-Heyrovsky mechanism and the excellent electrical conductivity provided by the integrated CNT framework. The Nyquist plots indicate that FeP@CNT-900-2 exhibits the lowest charge-transfer resistance (R_{ct} ~ 1.29 Ω) among all samples, confirming rapid electron migration across the electrode-electrolyte interface (Fig. 5c). This low R_{ct} is directly linked to the intimate contact between FeP NPs and CNTs, which minimizes interparticle resistance and accelerates the desorption of H_2 bubbles from the catalyst surface [60,61]. The chronopotentiometric stability profile at a high current density of 500 mA cm^{-2} over 1000 h of continuous operation (25 °C) in alkaline seawater reveals negligible voltage drift, underscoring the outstanding corrosion resistance and structural robustness of the catalyst (Fig. 5d and e). The interconnected CNT framework provides a highly conductive and mechanically robust network that firmly anchors the FeP NPs. This structure effectively suppresses NPs aggregation and oxidation, thereby ensuring long-term stability under high-current operation. Relative to previously reported non-precious metal electrocatalysts, the FeP@CNT-900-2 material validates both superior high-current-density performance and remarkable long-term stability, highlighting the distinct advantages and practical significance (Fig. 5e and Table S4). The O_2:H_2 evolution ratio remained stable at 1:2, confirming nearly 100% Faradaic efficiency (insert Fig. 5d). Post-stability polarization curves display only slight deviation from the initial measurements (Fig. S28), confirming the long-term retention of catalytic activity and the exceptional resilience of the FeP@CNT-900-2 heterostructure against chloride-induced degradation. To further examine the possible formation of chlorine-containing byproducts, the electrolyte collected after the long-term stability test was analyzed by UV–Vis spectroscopy (Fig. S29). No additional absorption features attributable to chlorine-containing species were observed compared with the fresh electrolyte, suggesting that oxygen evolution is the predominant anodic reaction under the investigated alkaline seawater conditions. Fig. 5f,g demonstrate the practical operation of the FeP@CNT-900-2 seawater electrolysis device under real outdoor environments using both solar power and a small battery. In Fig. 5f_1-f_4, continuous and uniform bubble generation at both electrode materials confirms efficient HER and OER activity, demonstrating that the catalyst maintains low overpotential and rapid charge transfer even under natural sunlight. Fig. 5g_1-g_3 further shows a portable setup that continuously generates gas without structural degradation of the materials, highlighting the strong stability of FeP@CNT-900-2 in natural seawater. Overall, Figs. 5f and 5 g (see also Video S1 and S2) demonstrate the consistent outdoor performance of the system and highlight the suitability of FeP@CNT-900-2 for practical, solar-driven seawater H_2 production, exhibiting the applicability of synthesized FeP@CNT-900-2 in various electrochemical applications [62].

3.2.3. Post materials analysis

The XRD pattern (Fig. S30a) confirms the formation of crystalline Fe_2P and Fe_3P phases, with minor changes after long-term alkaline seawater electrolysis, showing the structural strength and chemical durability of the FeP@CNT-900-2 heterostructure. Small shifts in the carbon-related peak (26.24°) indicate slight graphitic restructuring, indicating that the CNT framework maintains its crystallinity while increasing conductivity. FE-SEM (Fig. S30b, c) and TEM (Fig. S30d) images show that FeP NPs sustain consistent polyhedral morphology, regularly dispersed within the CNT network, which prevents aggregation and facilitates efficient charge transport and electrolyte diffusion. HRTEM (Fig. S30e) exhibits a core-shell structure, where the FeP NPs essentially provide active catalytic sites and the CNT shell confirms corrosion resistance, electrical continuity, and mechanical reinforcement, minimizing charge-transfer resistance. EDS analysis (Fig. S30f) proves the presence of Fe, P, C, N, and O, confirming successful hybridization with slight surface oxidation, leading to passivation. The XPS analysis of the FeP@CNT-900-2 catalyst provides detailed insights into the surface chemical states and composition before and after long-term alkaline seawater electrolysis, highlighting the material's robustness under harsh conditions.

In the Fe 2p spectra (Fig. S31a), the dominant peaks corresponding to Fe^{2+} and Fe^{3+} confirm that the FeP core mostly maintains its oxidation state, with only the least surface oxidation ensuing in prolonged operation. The P 2p XPS spectrum (Fig. S31b) of FeP@CNT-900-2 after OER shows a peak at ~133 eV, corresponding to surface phosphate-like PO_4^{2-}/PO_4^{3-} species, indicating partial oxidation of FeP and surface reconstruction under OER conditions [63], while the bulk FeP remains preserved. The C 1 s spectra (Fig. S31c) reveal a slight reorganization of the graphitic carbon, suggesting that the CNT framework provides excellent electronic conductivity while requiring mechanical support. The O 1 s and N 1 s spectra (Fig. S31d and e) establish the presence of minor oxygen species and nitrogen functionalities, which probably contribute to surface passivation, enhancing corrosion resistance and long-term stability in alkaline seawater. Together, the observations demonstrate that the FeP@CNT-900-2 catalyst possesses a well-engineered structure that combines structural integrity, high conductivity, and interfacial interaction, resulting in excellent bifunctional activity and durability for overall water splitting in challenging seawater conditions.

The HER activity is strongly governed by the Gibbs free energy of hydrogen adsorption (ΔG_{H^*}) and the adsorption capability toward H_2O molecules on the catalyst surface. As shown in Fig. 6a, the calculated ΔG_{H^*} values of Fe_2P (110) and Fe_3P (211) are −0.1021 and − 0.1156 eV, respectively, which are very close to that of the benchmark Pt catalyst (−0.1 eV) and the ideal thermoneutral value (0 eV). These results indicate that both surfaces possess highly favorable hydrogen

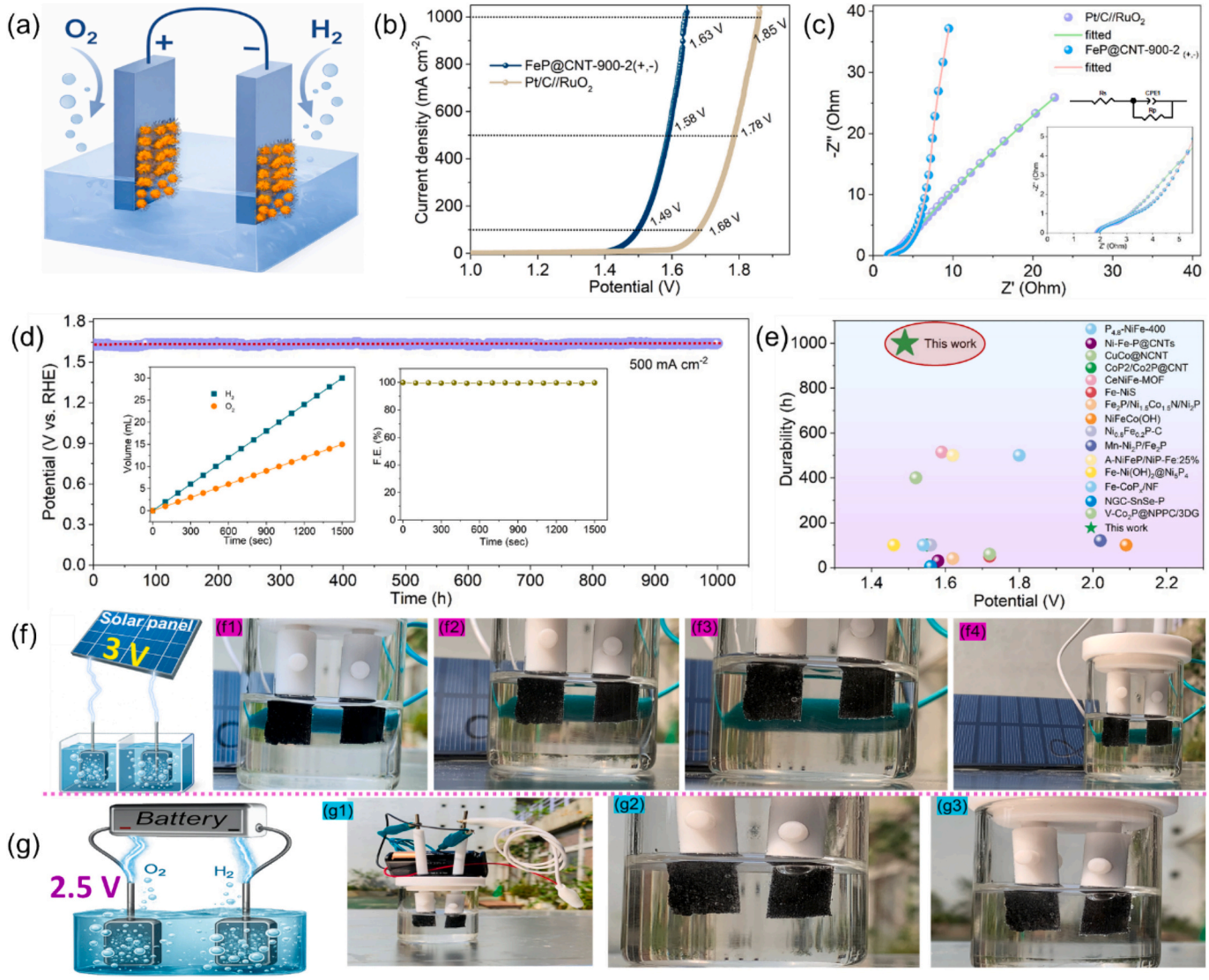

Fig. 5. (a) Schematic illustration of the seawater electrolyzer using the prepared FeP@CNT-900-2 catalysts as both the anode and cathode. (b) LSV curves of the FeP@CNT-900-2, (c) EIS spectra, (d) durability test of the electrolysis performed at a constant current density of 500 mA cm^{-2} at 25 °C (periodic electrolyte replenishment to maintain constant concentration), (e) comparison diagram of potential with stability, and (f, g) outdoor demonstration of solar- and battery-powered seawater electrolysis using FeP@CNT-900-2 symmetric electrodes.

adsorption/desorption characteristics for the HER process. However, despite the near-optimal ΔG_{H^*} value, Fe_2P (110) exhibits relatively weak H_2O adsorption with an adsorption energy of only −0.2055 eV (Fig. 6b), implying limited formation of the catalyst-H_2O intermediate during the initial water dissociation step. In contrast, Fe_3P (211) shows substantially stronger H_2O adsorption (−0.4519 eV) while maintaining a near-ideal ΔG_{H^*} value, suggesting balanced energetics for both water activation and hydrogen evolution. Therefore, Fe_3P (211) is considered to be the dominant active surface for HER, whereas Fe_2P (110) is expected to contribute only limitedly to the overall HER activity. The electronic origin of the stronger H_2O adsorption on the Fe_3P (211) surface is further investigated using differential charge density analysis. As shown in Fig. 6c, a significantly broader and more pronounced electron accumulation region (yellow cloud) is formed at the interfacial region between the adsorbed H_2O molecule and the Fe_3P (211) surface compared with that of Fe_2P (110) shown in Fig. 6d. In contrast, the charge redistribution on the Fe_2P (110) surface is relatively localized and weaker around the adsorption site. The optimized surface structure shows strong interfacial interaction and stable adsorption of the reaction intermediate at the active site, which can facilitate charge transfer and improve reaction kinetics (Fig. 6e, Fig. S32, S33). The results indicate that the Fe_3P (211) surface induces stronger electronic interaction and charge transfer with the adsorbed H_2O molecule, thereby leading to enhanced H_2O adsorption strength.

4. Conclusion

In this work, FeP@CNT-900-2, derived from ZnFe-MOF via a controlled PhosPy process, is demonstrated as a high-performance bifunctional catalyst for overall alkaline seawater splitting. The material exhibits remarkably low overpotentials of 74 mV for the HER and 184 mV for the OER at 10 mA cm^{-2}, along with outstanding stability of 200 h for each half-reaction under continuous operation. In a symmetric two-electrode configuration, the FeP@CNT-900-2||FeP@CNT-900-2 cell delivers a current density of 100 mA cm^{-2} at an exceptionally low cell voltage of 1.49 V, surpassing the benchmark Pt/C||RuO_2 system (1.68 V). It sustains continuous operation for 1000 h without any measurable loss in performance. This outstanding stability in chloride-rich seawater is enabled by the unique FeP-CNT heterostructure and pores, which not only accelerate charge transfer but also mitigate chlorine-related

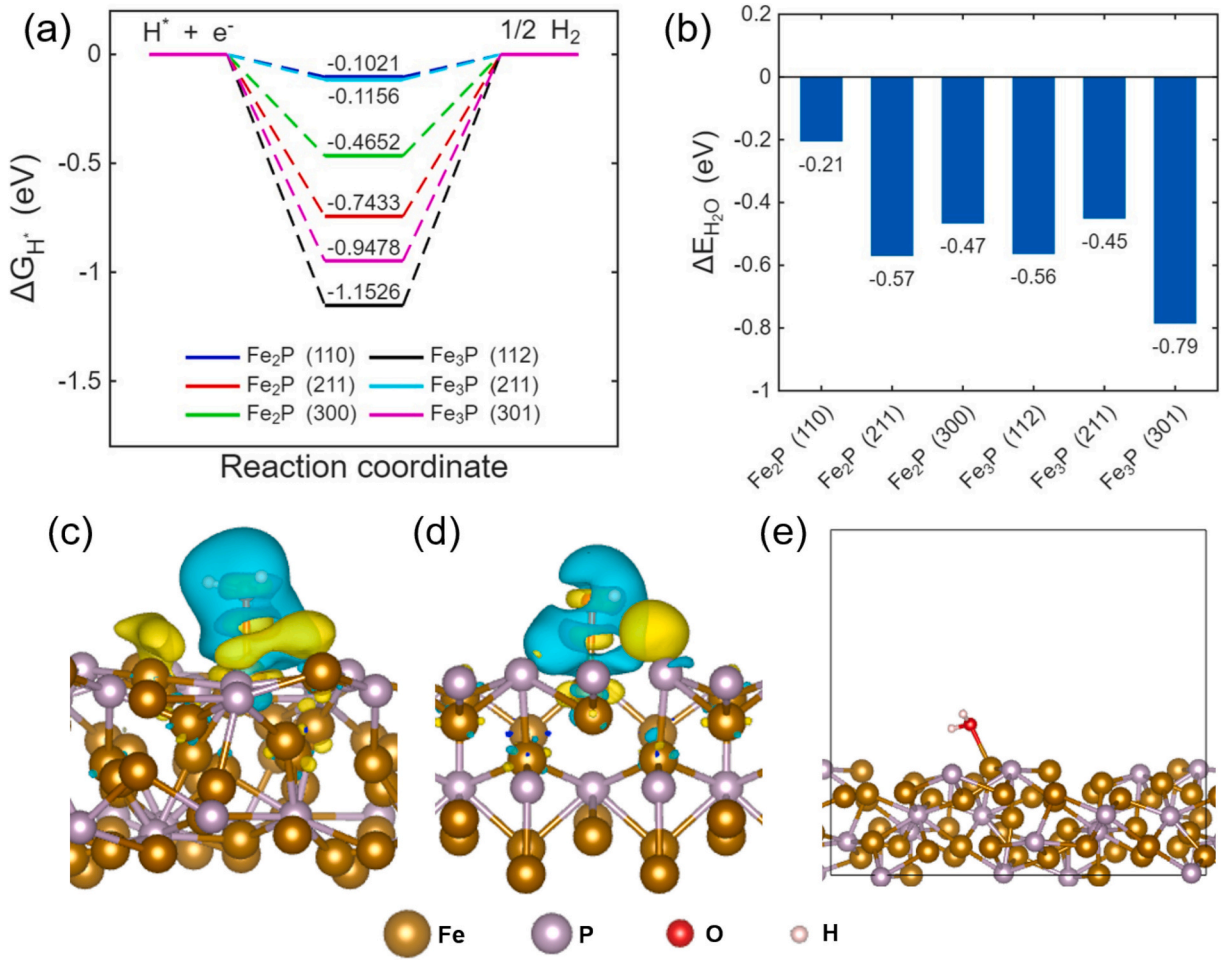

Fig. 6. (a) Free energy profile for HER, (b) H_2O adsorption energy, (c) Differential charge density distribution around the H_2O molecule adsorbed on Fe_3P (211), (d) Differential charge density distribution around the H_2O molecule adsorbed on Fe_2P (011), and (e) Atomic configuration of H_2O adsorption (301).

degradation. The phosphide phase promotes preferential OH^- adsorption over Cl^- at active Fe sites, effectively suppressing the ClER. Meanwhile, the CNT scaffold forms a conductive and hydrophobic barrier that hinders Cl^- penetration, while surface reconstruction under anodic bias generates a thin, robust FeOOH/FeP_x layer that passivates the interface against Cl^-. This cooperative protection mechanism both prevents Cl_2 gas generation and maintains catalytic integrity during prolonged operation. Collectively, these attributes establish FeP@CNT-900-2 as a novel, scalable, and seawater-compatible bifunctional electrocatalyst that represents an advanced design paradigm for industrial-scale, energy-efficient H_2 production directly from seawater, while effectively mitigating chlorine evolution.

CRediT authorship contribution statement

Samikannu Prabu: Writing – original draft, Methodology, Investigation. **Giwon Lee:** Validation, Methodology. **Mohan Reddy Pallavolu:** Validation. **Jinhan Cho:** Writing – review & editing. **Yong Nam Ahn:** Visualization, Validation. **Sungjun Park:** Writing – review & editing, Methodology. **Daegun Kim:** Writing – review & editing, Supervision, Funding acquisition.

Declaration of competing interest

The authors declare that they have no known competing financial interests or personal relationships that could have appeared to influence the work reported in this paper.

Acknowledgments

This study was supported by the National Research Foundation of Korea (NRF) grant funded by the Korea government (MSIT) (RS-2025-00516030, RS-2025-25413074, RS-2025-23525005, RS-2025-16069325, RS-2026-25483902). The fabrication and analysis of the samples was carried out using equipment supported by NFEC (No. NFEC-2025-02-303177 and NFEC-2024-12-301798).

Appendix A. Supplementary data

Supplementary data to this article can be found online at https://doi.org/10.1016/j.cej.2026.180631.

Data availability

Data will be made available on request.

References

[1] Z. Geng, Z. He, Y. Huang, Y. Li, X. Zhong, W. Deng, G. Zou, Y. Zhu, L. Tian, M. Guo, H. Hou, X. Ji, Recent advances on graphene quantum dots and their derivatives for energy storage devices, Int. J. Extreme Manuf. 8 (2026) 022005, https://doi.org/10.1088/2631-7990/ae2221.

[2] Y. Fan, S. Zhang, X. Ye, J. Zhou, Q. Kong, J. Zhang, Y. Long, J. Wang, Z. Hu, L. Zhang, Unique single-phase electrocatalyst for excellent overall water splitting facilitated by multi-atom synergistic effects, InfoMat 7 (2025) e70053, https://doi.org/10.1002/inf2.70053.

[3] Z. Li, Y. Liu, J. Hu, W. Luo, Y. Wang, Z. Xin, Y. Jia, Y. Pang, H. Zhang, Z.L. Zhao, Y. Li, Q. Wang, RuO_2 sub-nanocluster decorated Co_3O_4 as efficient and pH-

universal oxygen evolution electrocatalyst, InfoMat 7 (2025) e70003, https://doi.org/10.1002/inf2.70003.
[4] M. Rafiq, Z. Huang, C. Pi, L. Hu, F. Lu, K. Huo, P.K. Chu, Designing electrocatalysts for high-current-density freshwater/seawater splitting, Renewables 2 (2024) 2–24, https://doi.org/10.31635/renewables.023.202300043.
[5] Y. Zhao, Z. Yu, A. Ge, L. Liu, J.L. Faria, G. Xu, M. Zhu, Direct seawater splitting for hydrogen production: recent advances in materials synthesis and technological innovation, Green Energy Environ. 10 (2025) 11–33, https://doi.org/10.1016/j.gee.2024.02.001.
[6] X. Xu, Y. Zhong, M. Wajrak, T. Bhatelia, S.P. Jiang, Z. Shao, Grain boundary engineering: an emerging pathway toward efficient electrocatalysis, InfoMat 6 (2024) e12608, https://doi.org/10.1002/inf2.12608.
[7] Q. Shi, C. Zhu, D. Du, Y. Lin, Robust noble metal-based electrocatalysts for oxygen evolution reaction, Chem. Soc. Rev. 48 (2019) 3181–3192, https://doi.org/10.1039/C8CS00671G.
[8] Y. Yang, D. Chen, S. Hu, P. Pei, X. Xu, Advanced Ir-based alloy electrocatalysts for proton exchange membrane water electrolyzers, Small 21 (2025) e2410372, https://doi.org/10.1002/smll.202410372.
[9] D. Kim, H. Kim, J. Seo, I. Jeon, H. Lee, B. Kang, Recent trends in conjugated polymer-based thermoelectrics from materials to device, Ecomat 7 (2025) e70029, https://doi.org/10.1002/eom2.70029.
[10] L.K. Putri, B.-J. Ng, R.Y.Z. Yeo, W.-J. Ong, A.R. Mohamed, S.-P. Chai, Engineering nickel phosphides for electrocatalytic hydrogen evolution: a doping perspective, Chem. Eng. J. 461 (2023) 141845, https://doi.org/10.1016/j.cej.2023.141845.
[11] S. Ligani Fereja, A. Mehmood, Q. Ji, W. Raza, A. Hussen, J. Hu, S. Zhai, X. Cai, Advancing the utilization of 2D materials for electrocatalytic seawater splitting, InfoMat 7 (2025) e12623, https://doi.org/10.1002/inf2.12623.
[12] K. Jang, H. Yoon, J.S. Hyoung, D.S.A. Pratama, C.W. Lee, D.-W. Kim, Enhancement of hydrogen evolution activity by tailoring the electronic structure in ruthenium-heteroatom-doped cobalt iron phosphide nanoframes, Appl. Catal. B 341 (2024) 123327, https://doi.org/10.1016/j.apcatb.2023.123327.
[13] J. Lee, J. Lee, Recent developments in manganese-based materials for acidic oxygen evolution catalysis, Korean J. Chem. Eng. 42 (2025) 3333–3347, https://doi.org/10.1007/s11814-025-00512-2.
[14] H. Liu, W. Shen, H. Jin, J. Xu, P. Xi, J. Dong, Y. Zheng, S. Qiao, High-performance alkaline seawater electrolysis with anomalous chloride promoted oxygen evolution reaction, Angew. Chem. Int. Ed. 62 (2023) e202311674, https://doi.org/10.1002/anie.202311674.
[15] D. Yao, C. Liu, Y. Zhang, S. Wang, Y. Nie, M. Qiao, D. Zhu, Modulating selectivity and stability of the direct seawater electrolysis for sustainable green hydrogen production, Mater. Today Catal. 8 (2025) 100089, https://doi.org/10.1016/j.mtcata.2025.100089.
[16] J. Kim, J.H. Seo, J.K. Lee, M.H. Oh, H.W. Jang, Challenges and strategies in catalysts design towards efficient and durable alkaline seawater electrolysis for green hydrogen production, Energy Mater. 5 (2025) 500076, https://doi.org/10.20517/energymater.2024.220.
[17] W. Su, I. Munina, G. Cappelli, A. Sasnauskas, W. Zhang, W. Yuan, S. Ruan, G. O'Donnell, S. Yin, J.G. Lunney, R. Lupoi, High throughput inkless printing using laser produced dry aerosols, Int. J. Extreme Manuf. 8 (2026) 015511, https://doi.org/10.1088/2631-7990/ae02ff.
[18] J.-G. Choi, S. Baek, J. Lee, S. Park, Scalable metal-based nanoparticle synthesis via laser ablation in liquids for transformative sensory and synaptic devices, Int. J. Extreme Manuf. 7 (2025) 062001, https://doi.org/10.1088/2631-7990/ade836.
[19] W. Wang, D. Chen, F. Li, X. Xiao, Q. Xu, Metal-organic-framework-based materials as platforms for energy applications, Chem 10 (2024) 86–133, https://doi.org/10.1016/j.chempr.2023.09.009.
[20] T. Zhang, T. Yang, B. Li, S. Wei, W. Gao, MOF-derived formation of ultrafine FeP nanoparticles confined by N/P co-doped carbon as an efficient and stable electrocatalyst for hydrogen evolution reaction, Appl. Surf. Sci. 597 (2022) 153662, https://doi.org/10.1016/j.apsusc.2022.153662.
[21] H. Zhang, A. Chen, Z. Bi, X. Wang, X. Liu, Q. Kong, W. Zhang, L. Mai, G. Hu, MOF-on-MOF-derived ultrafine Fe 2 P-co 2 P Heterostructures for high-efficiency and durable anion exchange membrane water Electrolyzers, ACS Nano 17 (2023) 24070–24079, https://doi.org/10.1021/acsnano.3c09020.
[22] J. Xie, F. Wang, Y. Zhou, Y. Dong, Y. Chai, B. Dong, Internal polarization field induced hydroxyl spillover effect for industrial water splitting Electrolyzers, Nano Micro Lett. 16 (2024) 39, https://doi.org/10.1007/s40820-023-01253-9.
[23] J. Jin, J. Won, D. Kim, S.K. Arumugasamy, S. Park, T.-W. Kim, Integrated circuits on Fiber substrates: state-of-the-art system-on-Fiber Technologies for Smart Textiles and Wearables, Nano Micro Lett. 18 (2026) 232, https://doi.org/10.1007/s40820-025-02056-w.
[24] H. Yu, L. Qi, Y. Hu, Y. Qu, P. Yan, T.T. Isimjan, X. Yang, Nanowire-structured FeP-CoP arrays as highly active and stable bifunctional electrocatalyst synergistically promoting high-current overall water splitting, J. Colloid Interface Sci. 600 (2021) 811–819, https://doi.org/10.1016/j.jcis.2021.05.074.
[25] W. Xia, M. Ma, X. Guo, D. Cheng, D. Wu, D. Cao, Fabricating Ru atom-doped novel FeP4/Fe2PO5 heterogeneous Interface for overall water splitting in alkaline environment, ACS Appl. Mater. Interfaces 15 (2023) 44827–44838, https://doi.org/10.1021/acsami.3c07326.
[26] M. Gao, P. Gao, T. Lei, C. Ouyang, X. Wu, A. Wu, Y. Du, PANI-coated porous FeP sheets as bifunctional electrocatalyst for water splitting, Colloids Surf. A Physicochem. Eng. Asp. 651 (2022) 129673, https://doi.org/10.1016/j.colsurfa.2022.129673.
[27] J. Chang, Z. Hu, D. Wu, F. Xu, C. Chen, K. Jiang, Z. Gao, Prussian blue analog-derived nickel iron phosphide-reduced graphene oxide hybrid as an efficient catalyst for overall water electrolysis, J. Colloid Interface Sci. 638 (2023) 801–812, https://doi.org/10.1016/j.jcis.2023.02.037.
[28] D. Kim, S. Park, B. Yan, H. Hong, Y. Cho, J. Kang, X. Qin, T. Yoo, Y. Piao, Synthesis of remarkably thin co–Fe phosphide/carbon Nanosheet for enhanced oxygen evolution reaction Electrocatalysis driven by readily generated active Oxyhydroxide, ACS Appl. Energy Mater. 5 (2022) 2400–2411, https://doi.org/10.1021/acsaem.1c02023.
[29] S. Dresp, T. Ngo Thanh, M. Klingenhof, S. Brückner, P. Hauke, P. Strasser, Efficient direct seawater electrolysers using selective alkaline NiFe-LDH as OER catalyst in asymmetric electrolyte feeds, Energy Environ. Sci. 13 (2020) 1725–1729, https://doi.org/10.1039/D0EE01125H.
[30] Y. Kuang, M.J. Kenney, Y. Meng, W.-H. Hung, Y. Liu, J.E. Huang, R. Prasanna, P. Li, Y. Li, L. Wang, M.-C. Lin, M.D. McGehee, X. Sun, H. Dai, Solar-driven, highly sustained splitting of seawater into hydrogen and oxygen fuels, Proc. Natl. Acad. Sci. 116 (2019) 6624–6629, https://doi.org/10.1073/pnas.1900556116.
[31] L. Yu, Q. Zhu, S. Song, B. McElhenny, D. Wang, C. Wu, Z. Qin, J. Bao, Y. Yu, S. Chen, Z. Ren, Non-noble metal-nitride based electrocatalysts for high-performance alkaline seawater electrolysis, Nat. Commun. 10 (2019) 5106, https://doi.org/10.1038/s41467-019-13092-7.
[32] M. Yu, J. Li, F. Liu, J. Liu, W. Xu, H. Hu, X. Chen, W. Wang, F. Cheng, Anionic formulation of electrolyte additive towards stable electrocatalytic oxygen evolution in seawater splitting, J. Energy Chem. 72 (2022) 361–369, https://doi.org/10.1016/j.jechem.2022.04.004.
[33] S. Yin, Z. Zhai, F. Guan, Z. Ning, Z. Sun, J. Wu, W. Jiang, L. Luo, S. Yin, Suppressing oxygen-vacancy-mediated chlorine corrosion for high-current stable seawater electrolysis, Chem. Sci. (2025) 214–224, https://doi.org/10.1039/D5SC07816D.
[34] W. Xu, Z. Wang, P. Liu, X. Tang, S. Zhang, H. Chen, Q. Yang, X. Chen, Z. Tian, S. Dai, L. Chen, Z. Lu, Ag nanoparticle-induced surface chloride immobilization strategy enables stable seawater electrolysis, Adv. Mater. 36 (2024) 2306062, https://doi.org/10.1002/adma.202306062.
[35] Z. Chen, Q. Li, H. Xiang, Y. Wang, P. Yang, C. Dai, H. Zhang, W. Xiao, Z. Wu, L. Wang, Hierarchical porous NiFe-P@NC as an efficient electrocatalyst for alkaline hydrogen production and seawater electrolysis at high current density, Inorg. Chem. Front. 10 (2023) 1493–1500, https://doi.org/10.1039/D2QI02703H.
[36] J. Li, Y. Hu, X. Huang, Y. Zhu, D. Wang, Bimetallic phosphide heterostructure coupled with ultrathin carbon layer boosting overall alkaline water and seawater splitting, Small 19 (2023) 2206533, https://doi.org/10.1002/smll.202206533.
[37] C. Feng, Y. Zhou, S. Li, Y. Jin, M. Chen, R. Yang, W. Zhou, Z. Xie, X. Li, X. Chen, W. Lian, A. Abudula, G. Guan, An activity–selectivity–stability-balanced bifunctional high-entropy phosphide for overall seawater splitting at industrial-level current density, Green Chem. 27 (2025) 12785–12797, https://doi.org/10.1039/D5GC03723A.
[38] L. Wu, L. Yu, F. Zhang, B. McElhenny, D. Luo, A. Karim, S. Chen, Z. Ren, Heterogeneous bimetallic phosphide Ni_2P-Fe_2P as an efficient bifunctional catalyst for water/seawater splitting, Adv. Funct. Mater. 31 (2021) 2006484, https://doi.org/10.1002/adfm.202006484.
[39] X. Li, Z. Niu, M. Niu, J. Wang, D. Cao, X. Zeng, Single atom Ru doped Ni2P/Fe3P heterostructure for boosting hydrogen evolution for water splitting, Small 20 (2024) 2311335, https://doi.org/10.1002/smll.202311335.
[40] S. Prabu, J.S. Al-Otaibi, S. Pandiaraj, M.R. Pallavolu, K.-Y. Chiang, Synergistic effect of CoNiS@FeOOH hybrid nanostructured sheets for enhanced battery-type high energy density performance, ACS Appl. Energy Mater. 8 (2025) 10149–10161, https://doi.org/10.1021/acsaem.5c00903.
[41] S. Prabu, K.-Y. Chiang, A.N. Alodhayb, S. Pandiaraj, M.R. Pallavolu, Integrated electrode-electrolyte optimization to fabricate pinewood-derived carbon-permeated CoNi3S4(P) hybrid nanocomposites as redox-rich electrode materials for ultra-high energy density hybrid supercapacitors, J. Power Sources 640 (2025) 236705, https://doi.org/10.1016/j.jpowsour.2025.236705.
[42] R. Xing, T. Zhou, Y. Zhou, R. Ma, Q. Liu, J. Luo, J. Wang, Creation of triple hierarchical Micro-Meso-macroporous N-doped carbon shells with hollow cores toward the Electrocatalytic oxygen reduction reaction, Nano Micro Lett. 10 (2018) 3, https://doi.org/10.1007/s40820-017-0157-1.
[43] D. Schneider, D. Mehlhorn, P. Zeigermann, J. Kärger, R. Valiullin, Transport properties of hierarchical micro–mesoporous materials, Chem. Soc. Rev. 45 (2016) 3439–3467, https://doi.org/10.1039/C5CS00715A.
[44] S. Chen, L. Ma, Z. Huang, G. Liang, C. Zhi, In situ/operando analysis of surface reconstruction of transition metal-based oxygen evolution electrocatalysts, Cell Rep. Phys. Sci. 3 (2022) 100729, https://doi.org/10.1016/j.xcrp.2021.100729.
[45] C. Yue, X. Zhang, J. Yin, H. Zhou, K. Liu, X. Liu, Highly efficient FeS2@FeOOH core-shell water oxidation electrocatalyst formed by surface reconstruction of FeS2 microspheres supported on Ni foam, Appl. Catal. B 339 (2023) 123171, https://doi.org/10.1016/j.apcatb.2023.123171.
[46] P. Wang, J. Zheng, Y. Li, Q. Shi, J. Zhang, Y. Wan, M. Niu, Y. Yamauchi, Y. Long, Catalyst for industrial-scale seawater electrolysis: inhibit active metal dissolution and chlorine corrosion, Adv. Sci. 12 (2025) e14301, https://doi.org/10.1002/advs.202514301.
[47] P. Shen, J. Zhu, C. Deng, S. Zhu, X. He, W. Ouyang, X. Tu, H. Zhang, R. Lin, Dynamic stability in intermittent seawater electrolysis via frustrated Lewis pair engineering, Adv. Sci. 13 (2026) e18514, https://doi.org/10.1002/advs.202518514.
[48] K. Kim, D. Shin, E. Kim, D. Song, S.J. Lee, J. Bak, J. Roh, M. Kim, E. Cho, One-dimensional copper–iridium hollow nanotubes with an ultra-thin catalyst layer for enhanced oxygen evolution reaction, Korean J. Chem. Eng. 42 (2025) 3449–3458, https://doi.org/10.1007/s11814-025-00560-8.

[49] D.H. Powell, A.C. Barnes, J.E. Enderby, G.W. Neilson, P.S. Salmon, The hydration structure around chloride ions in aqueous solution, Faraday Discuss. Chem. Soc. 85 (1988) 137, https://doi.org/10.1039/dc9888500137.
[50] Y. Guan, H. Lu, L. Zhao, S. Zhu, Z. Cui, Z. Li, W. Xu, Z. Gao, T. Ba, Y. Liang, G. Long, H. Jiang, Interfacial electrostatic engineering for chlorine ions blocking toward long-lasting alkaline seawater oxidation, Small 21 (2025) e09149, https://doi.org/10.1002/smll.202509149.
[51] M. Chen, Y. Zhang, J. Chen, R. Wang, B. Zhang, B. Song, P. Xu, In situ Raman study of surface reconstruction of FeOOH/Ni_3S_2 oxygen evolution reaction electrocatalysts, Small 20 (2024) 2309371, https://doi.org/10.1002/smll.202309371.
[52] N. Shi, M. Gao, M. Maneesha, C.S. Praveen, P. Liu, S. Yue, W. Xie, D. Chen, Y. Tang, H. Fan, X. Huang, Unlocking the synergistic promoter role of phosphorus in evolving NiFe phosphides for enhanced water oxidation, Nano. Micro. Lett. 18 (2026) 400, https://doi.org/10.1007/s40820-026-02238-0.
[53] M.R. Pallavolu, S. Prabu, J.S. Al-Otaibi, S. Pandiaraj, G. Koyyada, T.V. M. Sreekanth, Integrated NiOOH@CoMnS hierarchical nanostructured electrocatalyst for sustainable hydrogen conversion *via* alkaline seawater electrolysis: synergistic design and mechanistic insights, J. Mater. Chem. A Mater. 13 (2025) 29218–29232, https://doi.org/10.1039/D5TA04643B.
[54] W. Yan, Z. Shi, H. Feng, J. Yu, W. Chen, Y. Chen, Crystalline metal phosphide-coated amorphous iron oxide-hydroxide (FeOOH) with oxygen vacancies as highly active and stable oxygen evolution catalyst in alkaline seawater at high current density, J. Colloid Interface Sci. 667 (2024) 362–370, https://doi.org/10.1016/j.jcis.2024.04.091.
[55] L. Su, X. Cui, T. He, L. Zeng, H. Tian, Y. Song, K. Qi, B.Y. Xia, Surface reconstruction of cobalt phosphide nanosheets by electrochemical activation for enhanced hydrogen evolution in alkaline solution, Chem. Sci. 10 (2019) 2019–2024, https://doi.org/10.1039/C8SC04589E.
[56] T. Chen, B. Li, K. Song, C. Wang, J. Ding, E. Liu, B. Chen, F. He, Defect-activated surface reconstruction: mechanism for triggering the oxygen evolution reaction activity of NiFe phosphide, J. Mater. Chem. A 10 (2022) 22750–22759, https://doi.org/10.1039/D2TA04879E.
[57] Z. Zuo, X. Zhang, O. Peng, L. Shan, S. Xiang, Q. Lian, N. Li, G. Mi, A. Amini, C. Cheng, Self-supported iron-based bimetallic phosphide catalytic electrode for efficient hydrogen evolution reaction at high current density, J. Mater. Chem. A Mater. 12 (2024) 5331–5339, https://doi.org/10.1039/D3TA06035G.
[58] S. Prabu, G. Nagaraju, S. Sengodan, K. Chiang, Highly stable bifunctional heterostructured electrocatalyst integrated with LDPE-derived spherical carbon for longevous alkaline seawater splitting, Small 21 (2025) 2500453, https://doi.org/10.1002/smll.202500453.
[59] Y. Yan, Q. Zheng, Y. Yan, S. Yan, Z. Zou, Highly durable Volmer-Heyrovsky hydrogen evolution reaction in alkaline media, J. Energy Chem. 113 (2026) 177–185, https://doi.org/10.1016/j.jechem.2025.09.037.
[60] S. Shaik, J. Kim, M.K. Kabiraz, F. Aziz, J.Y. Park, B.R. Anne, M. Li, H. Huang, K. M. Nam, D. Jo, S.-I. Choi, Rapid outgassing of hydrophilic TiO2 electrodes achieves Long-term stability of anion exchange membrane water Electrolyzers, Nano Micro Lett. 17 (2025) 186, https://doi.org/10.1007/s40820-025-01696-2.
[61] W. Zhou, Y. Huang, H. Cai, T. Wang, H. Li, C. Zhang, L. Zhao, L. Chen, M. Liao, Z. Tang, K. Chen, J. Gu, W. Gao, Z. Fan, Z. Wen, A strongly coupled cluster Heterostructure with Pt–N-Mo bonding for durable and efficient H2 evolution in anion-exchange membrane water Electrolyzers, Nano Micro Lett. 17 (2025) 296, https://doi.org/10.1007/s40820-025-01798-x.
[62] Z. Akbar, H. Liu, N. Zhang, P. Ming, H. Zhang, X. Luo, Frontiers in atomic-level manufacturing: atomic-scale electrochemical deposition, Int. J. Extreme Manuf. 7 (2025) 062008, https://doi.org/10.1088/2631-7990/adf6a3.
[63] N. Khodayar, A. Noori, M.S. Rahmanifar, M. Moloudi, N. Hassani, M. Neek-Amal, M.F. El-Kady, N.B. Mohamed, X. Xia, Y. Zhang, R.B. Kaner, M.F. Mousavi, An ultra-high mass-loading transition metal phosphide electrocatalyst for efficient water splitting and ultra-durable zinc–air batteries, Energy Environ. Sci. 17 (2024) 5200–5215, https://doi.org/10.1039/D4EE00042K.